Supporting Information

Tunable Out-of-Plane Piezoelectricity in Thin-Layered $MoTe_2$ by Surface Corrugation-Mediated Flexoelectricity

Seunghun Kang,[†] Sera Jeon,[‡] Sera Kim,[§] Daehee Seol,[†] Heejun Yang[§] Jaekwang Lee,[,‡] and Yunseok Kim[*,†]*

[†]School of Advanced Materials and Engineering, Sungkyunkwan University (SKKU), Suwon 16419, Republic of Korea

[‡]Department of Physics, Pusan National University, Busan, 46241, Republic of Korea

[§]Department of Energy Science, Sungkyunkwan University (SKKU), Suwon 16419, Republic of Korea

*E-mail: jaekwangl@pusan.ac.kr (J. L.), yunseokkim@skku.edu (Y. K.)

I. Calculation of Strain

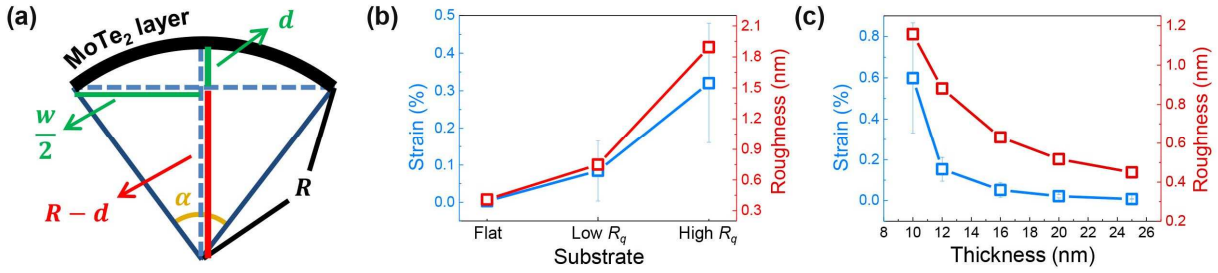

Figure S1. (a) Schematic of corrugated $MoTe_2$ layer and definition of each parameter in $MoTe_2$ layer for strain calculation. (b) Strain (left axis) and roughness (right axis) of $MoTe_2$ flake versus type of substrate. Strain and roughness of $MoTe_2$ flakes were obtained from Figures 2d–f. (c) Strain (left axis) and roughness (right axis) of the $MoTe_2$ flake versus its thickness. Strain and roughness of $MoTe_2$ flakes were obtained from the inset images of Figures 2g and the data of 12- and 25-nm-thick flakes was obtained from other flakes for the comparison. Strain in Figures (b) and (c) was calculated from 10–30 corrugated positions in each image, and roughness was calculated from the entire area of each measured image.

Based on the surface topography, the strain (ε) of the transferred $MoTe_2$ flake was calculated using the equation given below to understand the corrugation effect on the resulting $MoTe_2$ flake. For the strain calculation of the $MoTe_2$ flake, strain can be expressed by assuming a pan shape in the corrugated case from Equation S1:

$$Strain\ (\varepsilon) = \frac{Change\ in\ length\ (\Delta L)}{Original\ length\ (L)} (\times 100\%) = \frac{R\alpha - W}{W} (\times 100\%) \quad \text{(S1)}$$

where L and ΔL refer to the original length and the change in length in the corrugated layer, respectively, and W, R, and α are width, radius, and the angle of the arc as shown in Figure S1a, respectively. Since W and d can be determined from the line profile in each topography image, R

can be calculated by the Pythagorean theorem in each corrugated position. Then, Equation S1 can be written as follows:

$$Radius\ of\ curvature\ (R) = \frac{d^2 + (w/2)^2}{2d} \quad . \qquad (S2)$$

Also, α can be derived by Equation S3:

$$Angle\ of\ the\ arc\ (\alpha) = 2\arcsin\frac{(w/2)}{R} \quad . \qquad (S3)$$

Therefore, the strain values can be roughly calculated through the derivation process described above.

As shown in Figures S1b and c, we calculated the strain depending on substrate roughness and flake thickness. Even though this only shows the correlation between roughness and strain, the correlation between roughness and strain gradient is expected to be similar, because a high strain region will have a high strain gradient. It is evident that the flexoelectricity of $MoTe_2$ flakes are closely related to substrate roughness. Therefore, substrate roughness can be an effective parameter for controlling the degree of flexoelectricity.

II. Topography of $MoTe_2$ flake and Au substrate

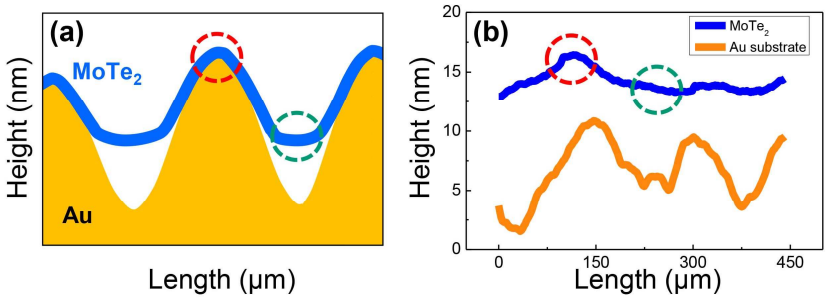

Figure S2. Schematics of the (a) local surface features and (b) line profiles of $MoTe_2$ flakes and Au substrate. The red and green circles indicate the peaks and the valleys of $MoTe_2$, respectively. Note that the line profiles of $MoTe_2$ and Au substrate are not extracted from the same position.

The topography of the $MoTe_2$ flake exfoliated on the Au substrate generally reflects that of the Au substrate, as schematically shown in Figure S2a. However, when the $MoTe_2$ flake was transferred onto the corrugated surface of Au, the portion of the flake spanning sharp valleys of the Au substrate may be locally suspended. Thus, the valley regions of the $MoTe_2$ flake can exhibit relative flatness (see red and green circles in Figure S2). Indeed, the $MoTe_2$ flake is smoother than the Au substrate (as evident from Figure S2b), and even though sharp peaks can be seen in Figure S2b, sharp valleys are barely visible. We note that the roughness of the $MoTe_2$ flake and Au substrate over the areas in which the line profiles were extracted are 1.06 nm and 2.62 nm, respectively. It is also noted that annealing could improve adhesion between the $MoTe_2$ flake and the substrate.

III. PFM signal in different thick $MoTe_2$ flakes

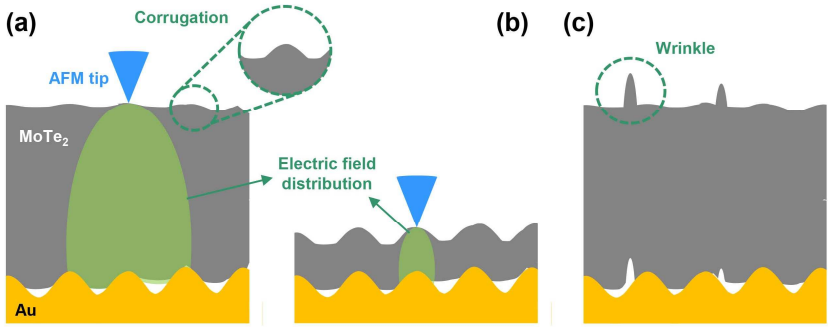

Figure S3. (a, b) Schematics for surface features and electric field distribution of $MoTe_2$ flakes depending on flake thickness: relatively (a) thick and (b) thin $MoTe_2$ flakes. (c) Schematic for surface features of thick $MoTe_2$ flakes with wrinkles.

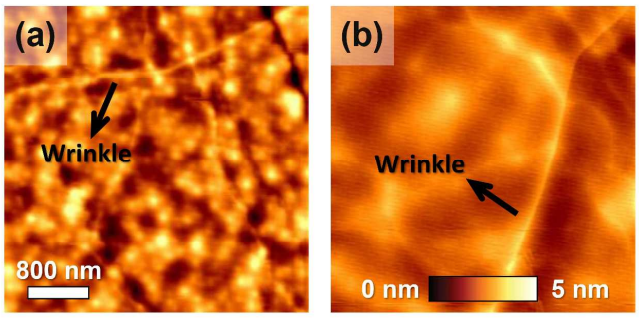

Figure S4. Topography images of (a) 25-nm and (b) 85-nm thick $MoTe_2$ flakes transferred on a high roughness substrate (R_q = 3.0 nm). The arrows indicate wrinkles.

In Figure 4d, the $d_{33,eff}$ was observed over the entire measured area without dot-like features. Even though the primary contribution to observed $d_{33,eff}$ might originate from electrostatic interaction, this might be partially related to the degree of the corrugation and the electric field distribution during the PFM measurements. Although the small degree of corrugation, *i.e.* very low roughness, on the surface does not allow current flow, out-of-plane

piezoelectricity can be still generated because, since the surface is not completely flat, the small degree of corrugation near the surface of thick $MoTe_2$ flakes contributes to the out-of-plane piezoelectricity (see the dotted circle in Figure S3a). Furthermore, the bottom part of the flake close to the substrate might be still affected by the substrate roughness (see Figure 3a). In such a situation, since the electric field distribution during the $d_{33,eff}$ measurements covers a relatively large area compared to that in the thin flake, the channeling features are hard to discern (see Figures S3a and b).

We note that, as shown in Figure S3c, wrinkles can be generated during the sample preparation (here, using mechanical exfoliation method), considering thickness relative to lateral size (> several μm) in the $MoTe_2$ flakes. Indeed, as presented in Figure S4, wrinkles were observed in some of $MoTe_2$ flakes. These wrinkles can generate additional out-of-plane PFM amplitude. However, since all the $d_{33,eff}$ measurements were performed in areas far from wrinkles or in flakes without wrinkles, we determined that this is not a major contribution.

IV. CAFM results

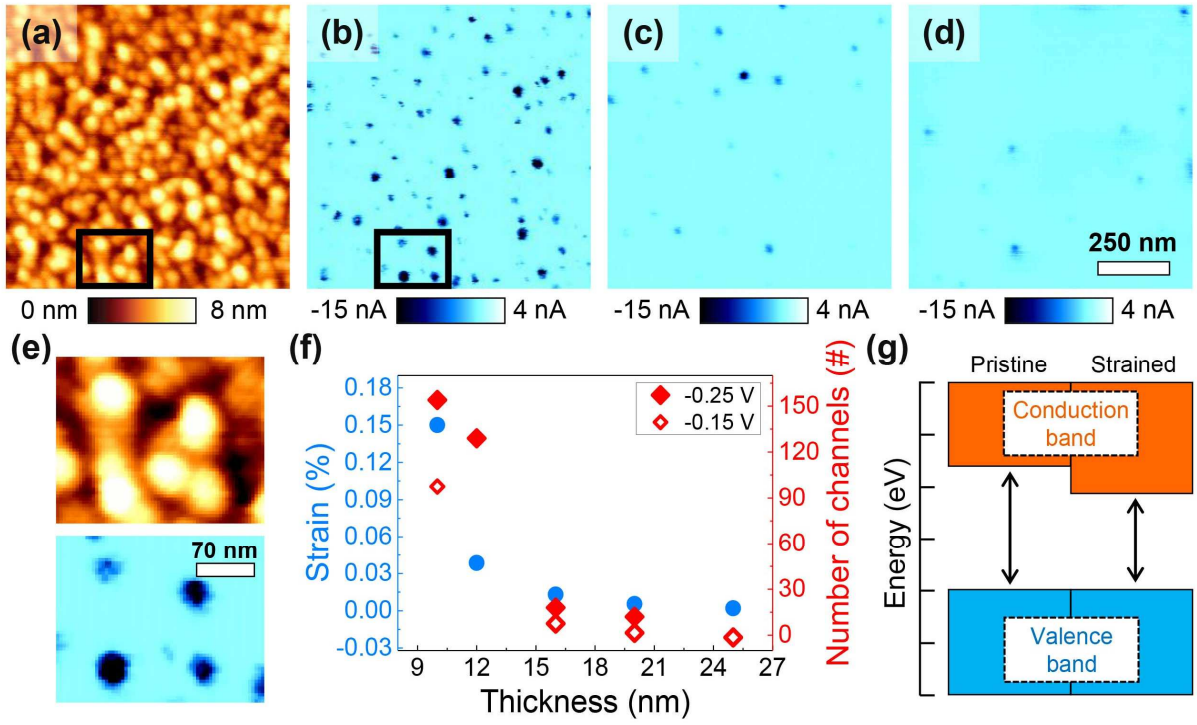

Figure S5. (a) Representative topography and (b-d) CAFM images at –0.25 V_{dc} corresponding to the inset topography images in Figure 2g: each flake thickness of the measured images is (a, b) 10 nm, (c) 16 nm, and (d) 20 nm, respectively. (e) Topography (top) and CAFM (bottom) images cropped from the black rectangle in Figures (a) and (b). (f) Strain in $MoTe_2$ flake (left axis) and the number of relatively conducting dots (right axis) as a function of $MoTe_2$ thickness. (g) Schematic of band alignment in pristine and strained 2H-$MoTe_2$.

The conductive atomic force microscopy (CAFM) images were measured using a current amplifier (Femto DLPCA-200). DC voltage (–0.15 or –0.25 V_{dc}) was applied to the AFM tip and the bottom electrode was used as a ground channel for measuring the current.

While strain gradient related flexoelectricity can induce out-of-plane piezoelectricity, strain can also induce changes in the electrical conductivity of the 2D TMDs.[1-4] Therefore, we

also examined the dependence of electrical conductivity on the corrugation by using CAFM. The CAFM images in Figures S5b–d were simultaneously measured with the topography images as presented in insets of Figure 2g. As expected, conducting channels were primarily observed on the corrugated regions. This was also observed in the enlarged images shown in Figure S5e. Furthermore, as shown in Figure S5f, the number of the relatively conducting dots gradually decreased as flake thickness increased (*i.e.*, the strain decreased). These results imply that strain induces changes in the electrical properties of $MoTe_2$ flakes. It is noted that corrugation engineering by modulating the substrate roughness also shows the same trend (not shown here). The variations in electrical conductivity can originate from changes in band gap due to strain, as schematically represented in Figure S5g (see the details in Figure S7 and S8). As can be expected from Figure S5f, the relatively conducting dots had vanished in sufficiently thick $MoTe_2$ flakes because the substrate roughness no longer significantly induced corrugation of the $MoTe_2$ flakes. However, we found that not all the brighter dots in the topography images show higher current. The locally different strain states can induce locally different electrical properties. Thus, under a certain dc voltage for measuring CAFM, the current contrast can be dependent on the local strain state. We also note that there could be non-linear effects on the Schottky barrier height such as Fermi-level pinning and/or interfacial contamination. Thus, the obtained CAFM results might be affected by the non-linear effects.

V. Theoretical calculations

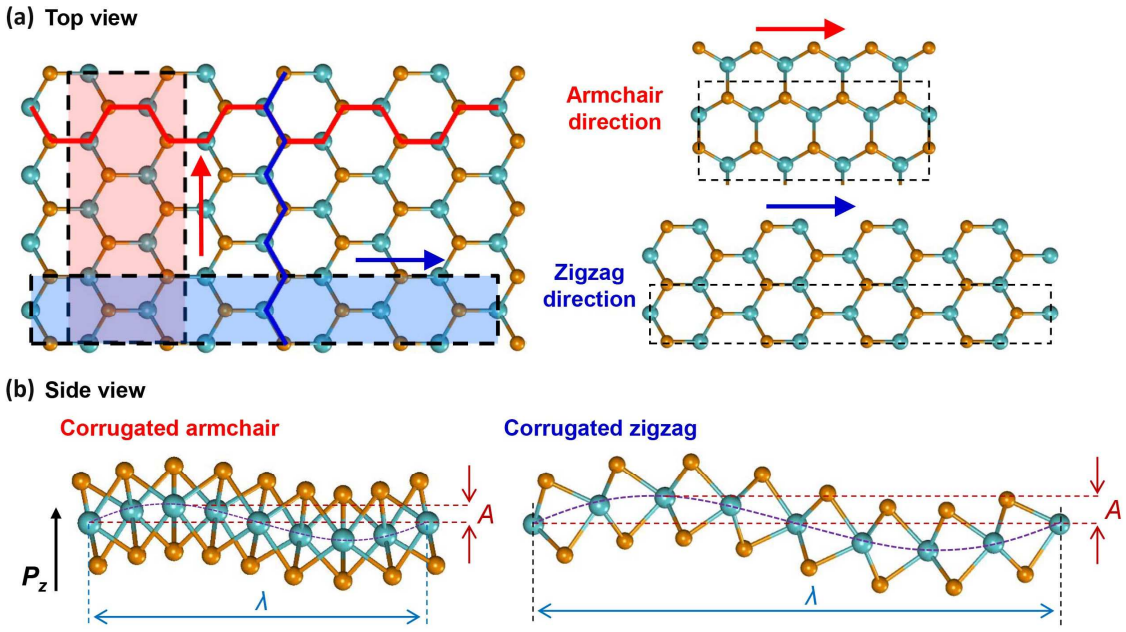

Figure S6. Schematic diagrams of the (a) top and (b) side view of possible corrugated crystal structures of 2H-$MoTe_2$ flakes, in armchair and zigzag directions. *A* and λ indicate the height and width of the corrugated structure, respectively.

The schematic diagram given in Figure S6 illustrates the structure of $MoTe_2$ and the two different pattern directions with strain. Since ultra-thin 2D TMDs have different electrical and mechanical properties depending on their direction in the structure,[5,6] we calculated both directions (although only one direction has been shown in the manuscript).

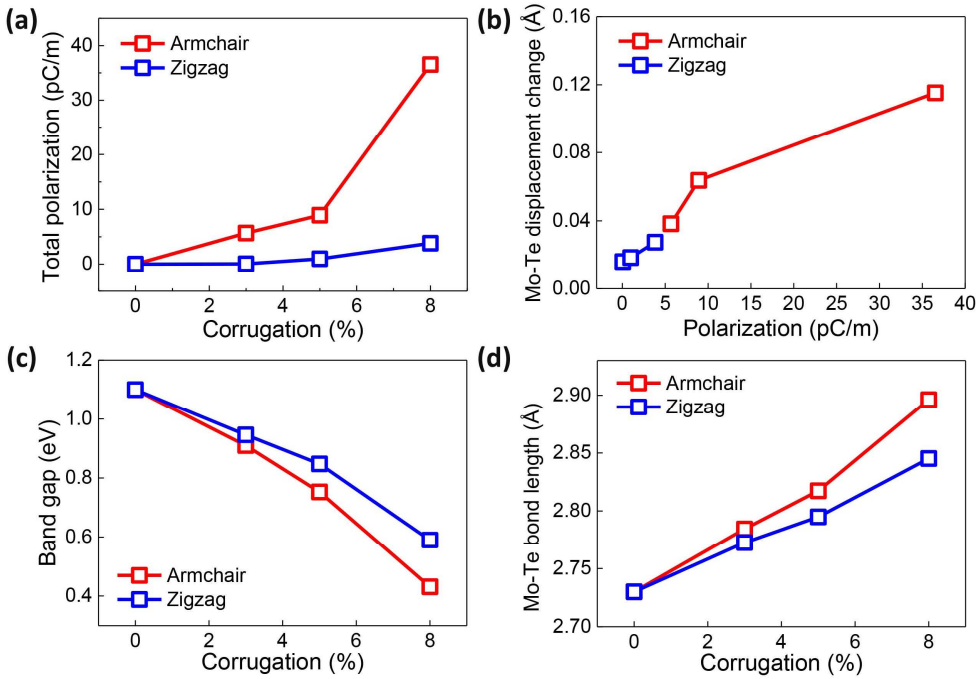

Figure S7. (a) Theoretical calculation of the total polarization depending on the corrugation in 2H-$MoTe_2$. (b) Displacement changes between the Mo and Te atoms in the molecular structure according to the magnitude of polarization in 2H-$MoTe_2$. (c, d) Theoretical calculation of the (c) band gap and (d) displacement changes between the Mo and Te atoms in the molecular structure depending on the corrugation in 2H-$MoTe_2$.

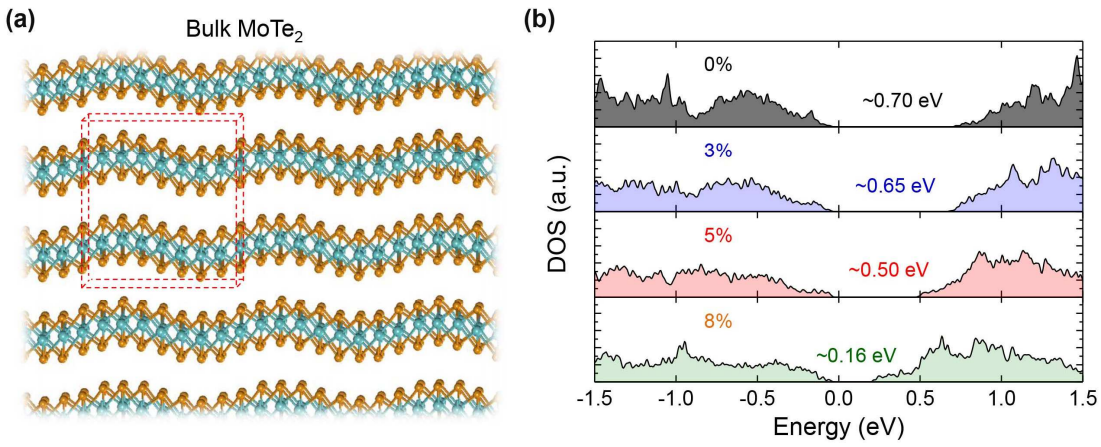

Figure S8. (a) Atomic structure of corrugated bulk $MoTe_2$ in the armchair direction and (b) bandgap change due to the corrugation in the density of states (DOS).

Figure S7 compares the armchair and zigzag-corrugated $MoTe_2$ structures. Zigzag corrugated $MoTe_2$ has a much smaller polarization compared to the armchair direction (Figure S7a). Figure S7b shows that the total out-of-plane polarization is approximately linearly proportional to the relative atomic displacement between Mo and Te along the out-of-plane direction induced by the corrugation. In particular, it was found that the Te atoms in the zigzag-corrugated structure move in the opposite in-plane direction, which decreases the relative atomic displacement between Mo and Te along the out-of-plane direction and consequently reduces the increase in out-of-plane polarization. On the other hand, the Te atoms in the armchair-corrugated structure move in the parallel in-plane direction, which increases the relative atomic displacement between Mo and Te along the out-of-plane direction and consequently intensifies the increase in out-of-plane polarization.

The electrical conductivity shown in Figure S5 can be primarily related to the decrease of the $MoTe_2$ band gap due to strain.[7] As shown in Figure S7, for the corrugated $MoTe_2$ (8% corrugation) of the armchair direction, the band gap is decreased to 0.4 eV, which is about 60%

reduction with respect to the band gap of pristine $MoTe_2$. Therefore, in the CAFM measurements with the corrugated $MoTe_2$, more electrons can be in the conduction band by such a huge reduction of the band gap, which can strongly influence the electrical property of the corrugated $MoTe_2$ system. Furthermore, as shown in Figure S8, the corrugation significantly reduces the band gap of bulk 2H-$MoTe_2$, which is consistent with the band gap decrease of monolayer $MoTe_2$ system due to corrugation. Moreover, the absolute value of the bang gap for the bulk was much smaller than that for the monolayer. Considering the previously reported band structures under tensile strain as well as the above results,[2, 8] the reduction of the band gap can be the primary origin for the increased current; the ambipolar semiconducting nature of 2H-$MoTe_2$ generates a smaller Schottky barrier height with a decreased band gap. Thus, in this case, the increased conductivity with the band gap change also involves the contact issue (by the Schottky barrier height).

Nonetheless, even though the theoretical results support strain-induced high conduction, the poor contact of the valleys as presented in Figure S2 can also induce conducting contrast shown in Figure S5. As a result, the CAFM results may be insufficient to prove the theoretically-expected scenario.

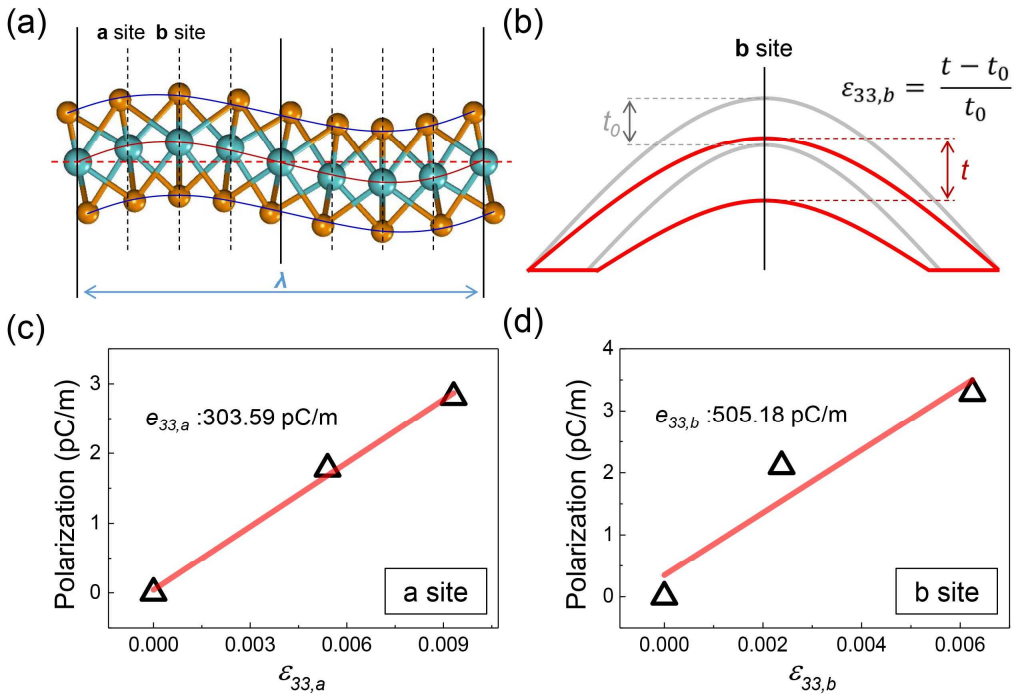

Figure S9. (a, b) Schematic drawings of (a) corrugated 2H-$MoTe_2$, indicating that corrugation amplitude is dependent on Mo atom site, and (b) *b* site out-of-plane strain. (c, d) Theoretical calculation for local piezoelectric coefficient $e_{33,loc}$ at the atomic positions of (c) the *a* site and (d) *b* site, respectively. Each data point is obtained at corrugation of 0, 3, and 5 %, respectively.

After lattice relaxation of corrugated 2H-$MoTe_2$, we observe that the layer thickness at the *b* site is changed from t_0 to t as indicated in Figure S9b, and the local out-of-plane strain at the *b* site ($\varepsilon_{33,b}$) is calculated from the difference between t_0 and t. The local out-of-plane strain at the *a* site ($\varepsilon_{33,a}$) can be also calculated in the same way. We found that the local out-of-plane strain ($\varepsilon_{33,loc}$) increases almost linearly with the degree of corrugation dependent on the Mo atomic sites.

The local electric polarization along the out-of-plane direction is approximated as $P_{3,loc} \sim e_{33,loc}\varepsilon_{33,loc}$ (Here, flexoelectric effect is effectively included into the elastic strain effect).

As a result, as shown in Figures S9c and d, the effective local piezoelectric coefficient $e_{33,loc}$ is obtained by linear interpolation between local polarization ($P_{3,loc}$) and local out-of-plane strain ($\varepsilon_{33,loc}$) depending on the Mo atomic site.

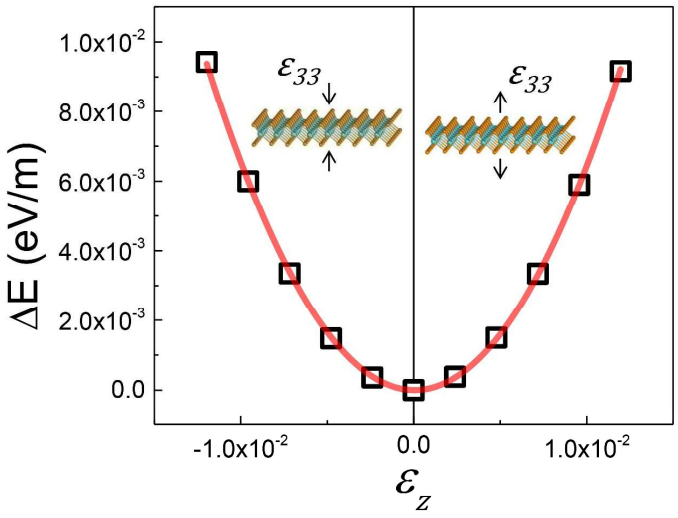

Figure S10. Theoretical calculation for elastic constant c_{33} of 2H $MoTe_2$.

We manually apply strain (ε_{33}) to the 2H-$MoTe_2$ along the out-of-plane direction as indicated in Figure S10, and the elastic constant c_{33} is determined to be 64.97 N/m from the curvature of the total energy change with respect to the out-of-plane strain.

From the linear relationship between the piezoelectric coefficient and the elastic constant, $e_{33,loc} = d_{33,loc}c_{33}$, the local piezoelectric coefficient $d_{33,loc}$ is calculated to be 2.34–3.89 pm/V, which is also dependent on the Mo atomic site as indicated in Figure S9a. Our theoretical values are similar to the experimental result of 3.98 pm/V. Differences between the results may be due to the layer thickness since the experimental result is obtained from multilayer $MoTe_2$, whereas the theoretical calculations are based upon monolayer $MoTe_2$. While the theoretical results are a little large, they are still the same order of magnitude as the experimental results.

References

1. Conley, H. J.; Wang, B.; Ziegler, J. I.; Haglund, R. F.; Pantelides, S. T.; Bolotin, K. I., Bandgap Engineering of Strained Monolayer and Bilayer MoS_2. *Nano Lett.* **2013,** *13*, 3626-3630.

2. Guzman, D. M.; Strachan, A., Role of Strain on Electronic and Mechanical Response of Semiconducting Transition-Metal Dichalcogenide Monolayers: An *Ab-Initio* Study. *J. Appl. Phys.* **2014,** 115, 243701.

3. Shen, T. T.; Penumatcha, A. V.; Appenzeller, J., Strain Engineering for Transition Metal Dichalcogenides Based Field Effect Transistors. *ACS Nano* **2016,** *10*, 4712-4718.

4. Shin, B. G.; Han, G. H.; Yun, S. J.; Oh, H. M.; Bae, J. J.; Song, Y. J.; Park, C. Y.; Lee, Y. H., Indirect Bandgap Puddles in Monolayer MoS_2 by Substrate-Induced Local Strain. *Adv. Mater.* **2016,** *28*, 9378-9384.

5. Ghorbani-Asl, M.; Borini, S.; Kuc, A.; Heine, T., Strain-Dependent Modulation of Conductivity in Single-Layer Transition-Metal Dichalcogenides. *Phys. Rev. B* **2013,** *87*, 235434.

6. Wei, W.; Dai, Y.; Sun, Q. L.; Yin, N.; Han, S. H.; Huang, B. B.; Jacob, T., Electronic Structures of In-Plane Two-Dimensional Transition-Metal Dichalcogenide Heterostructures. *Phys. Chem. Chem. Phys.* **2015,** *17*, 29380-29386.

7. Manzeli, S.; Allain, A.; Ghadimi, A.; Kis, A., Piezoresistivity and Strain-Induced Band Gap Tuning in Atomically Thin MoS_2. *Nano Lett.* **2015,** *15*, 5330-5335.

8. Lu, P.; Wu, X. J.; Guo, W. L.; Zeng, X. C., Strain-Dependent Electronic and Magnetic Properties of MoS_2 Monolayer, Bilayer, Nanoribbons and Nanotubes. *Phys. Chem. Chem. Phys.* **2012,** *14*, 13035-13040.